

# Topological edge states on time-periodically strained armchair graphene nanoribbons

Pedro Roman-Taboada\* and Gerardo G. Naumis

*Departamento de Sistemas Complejos, Instituto de Física,  
Universidad Nacional Autónoma de México (UNAM),  
Apartado Postal 20-364, 01000 México, Ciudad de México, México*

We report the emergence of electronic edge states in time-periodically driven strained armchair graphene nanoribbons. This is done by consider a short-pulse spatial-periodic strain field. Then, by using a chiral tight binding Hamiltonian the system is mapped into a one dimensional ladder akin to the Kitaev ladder. The time periodicity is thus considered within the Floquet formalism, and the quasienergy spectrum was analytically found for a particular case. Very interesting features were found. Firstly, the case system is able to support gapless and gapped phases. Secondly, very different edge states emerge for both the gapless and the gapful phases. In the case of the gapless phase, edge states emerge at the gap centered at zero quasienergy, although the Chern number is zero. For the gapless phase, besides edge states at zero quasienergy emerge, cosine like edge states which merge and coexist with the bulk band are observed. To confirm the topological nature of these edge states we analytically obtained the quasienergy spectrum for a particular case, finding that the edge states are topologically weak.

## I. INTRODUCTION

Topological insulators are materials which can support low energy excitations at the edges that are topologically protected<sup>1</sup>. Such low energy excitations have attracted a lot of attention due to their potential to be used in the field of topological quantum computing<sup>2,3</sup> or in spintronics<sup>4-6</sup>. After the experimental observation of topological insulators<sup>7,8</sup>, many systems exhibiting topologically non-trivial properties have been proposed<sup>9-25</sup>. Among them, one can mention the remarkable case of periodically driven systems, which have been proven to have very rich and newer interesting topological features when compared with the static topological case<sup>11,26,27</sup>. For instance, periodically driven systems can give rise to Majorana-like edge states<sup>28</sup>, chiral and counter-propagating edge states<sup>13</sup>, among many others<sup>29-33</sup>. The emergence of the edge states is protected by a conservation law or symmetry of the bulk system, this is the so-called bulk-edge correspondence<sup>34</sup>. The role played by the symmetries is fundamental to correctly describe the topological properties of these kind of systems, since they shed light about the topological invariant that can be used to describe these kind of systems<sup>35,36</sup>. Although great progress has been made in the topological classification of periodically driven gapful systems<sup>37,38</sup>, the topological classification of gapless systems is yet incomplete. For instance, the topological properties of Dirac semimetals cannot be described by the topological invariants used for gapful systems<sup>39</sup>.

On the other hand, one can mention graphene, a truly two dimensional crystal with extraordinary mechanical properties (that have given rise to very interesting phenomena in deformed graphene<sup>40-44</sup>), which is known to have a non-trivial topological behavior not only in the static case<sup>42,45-48</sup> but also in the periodically driven case<sup>25,49-51</sup>. Between them, for the time-dependent case, we have, for instance, chiral edge states<sup>13</sup>, flat bands<sup>25</sup>, Majorana-like edge modes<sup>52</sup>, and so on. Motivated by the

previous discussion, we decided to study the emergence of edge states in periodically driven uniaxial strained armchair graphene nanoribbons (AGNs) using a tight binding approach within the Floquet theory. It is worthwhile to mention that our system possesses chiral symmetry. In particular and in order to compared with other works, we have chosen to consider a spatial-periodic strain field. It is important to remark that the case here studied is fundamentally different from the one treated in a previous work, where we considered the case of a periodically driven strained zigzag graphene nanoribbon<sup>25</sup> (ZGN). The first and maybe the most important difference is that the AGN case can support gapless and gapful phases while the ZGN case can only support gapless phases, this is a consequence of static properties of strained graphene nanoribbons (see, for example, <sup>42,53,54</sup>). Second, the edge states nature of periodically driven strained AGN are completely different from the one observed in the ZGN case, see<sup>25</sup>. For instance, as we will see later on, for periodically driven AGN in the gapless phase, cosine-like edge states emerge, these states merge and coexist with the bulk bands. On the other hand, for the gapful phase, besides the edge states that appear in the gap centered at zero quasienergy, another edge states emerge in other gaps. This is interesting since it has been proven that for periodically driven chiral system, fully gaps around zero and  $\pm\pi$  quasienergies are topologically trivial from the Chern number point of view<sup>55</sup>. The implications of this fact are discussed below.

To finish, the paper is organized as follows, in section II, we describe the theoretical model and the notation to be used. In section III we analyze the quasienergy spectrum and the edge states for both the gapful and the gapless phases of our model. The topological properties of the edge states for both the gapless and the full gapped phase are discussed in section IV via the symmetries of the time evolution operator. In section V we study the topological nature of the edge states that emerge in the gapless phase via an effective Hamiltonian

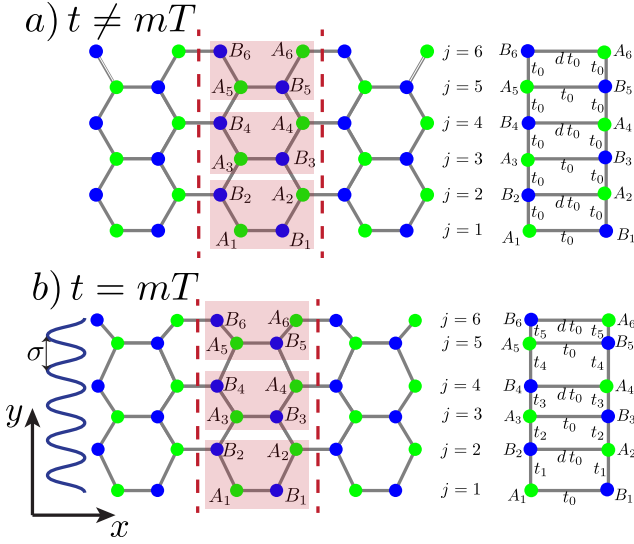


FIG. 1. (Color online). Schematic representation of the periodically delta driving layout for an armchair graphene nanoribbon. The strain field is turned on for  $t = mT$  as can be seen in panel b), here  $T$  is the period of the delta driving. For  $t \neq T$ , the strain field is turned off as shown in panel a). For uniaxial strain along the  $y$ -direction (in particular we consider sinusoidal strain with wavelength  $\sigma$ ), the strained armchair graphene nanoribbon can be mapped onto a one-dimensional effective system, which is represented by linear ladders on the left in the figure. Solid dots represent the position of carbon atoms.

approach. Some conclusions are proposed in section VI. Appendices A and B include some calculations concerning to the main text.

## II. PERIODICALLY DRIVEN STRAINED GRAPHENE

Consider a pristine armchair graphene nanoribbon (AGN) as the one shown in Fig. 1 b). Suppose that now we apply a spatially periodic strain field along the  $y$ -direction, given by

$$u(y_j) = \lambda \cos(2\pi\sigma y_j + \phi), \quad (1)$$

here  $\lambda$  is the amplitude,  $\sigma$  is the wavelength, and  $\phi$  the phase of the strain field.  $y_j$  are the positions of the carbon atoms along the  $y$ -direction inside the unit cell (see Fig. 1, therein the unit cell of the system is indicated by dotted red lines). The main advantage of uniaxial strain is the symmetry along the  $x$ -axis that allows to have a good quantum number associated, the quasimomentum along  $x$ -direction, that we denote by  $k_x$ . As a result, it is possible to decouple the two-dimensional system into an effective one-dimensional system<sup>41,42,56</sup>. In the tight binding limit, the electronic properties of graphene under an uniaxial strain field, as the one in Eq. (1), are described by the following one-dimensional (1D) effective

Hamiltonian<sup>42</sup>

$$H(k_x) = \sum_{j=1}^{N/2-1} \gamma_0 \left[ d(k_x) a_{2j}^\dagger b_{2j} + a_{2j-1}^\dagger b_{2j-1} \right] + \sum_{j=1}^{N/2-1} \gamma_j a_j^\dagger b_{j+1} + \text{h.c.}, \quad (2)$$

where  $d(k_x) = \exp(3i k_x a)$ ,  $k_x$  is the crystal momentum in the  $x$ -direction and  $a$  is the interatomic distance between carbon atoms in unstrained graphene. In what follows, we will set  $a = 1$  and thus all momenta  $k_x$  are measured in units of  $a$ . Also,  $N$  is the number of atoms per unit cell and  $a_j$  ( $b_j$ ) annihilates an electron at the site  $j$  in the sub lattice A (B), see Fig. 1. The hopping parameters are given by,

$$\frac{\gamma_j}{\gamma_0} = \exp \left[ \beta \left( \sqrt{1 - \lambda\sqrt{3}f(j, \sigma, \phi) + \lambda^2 f^2(j, \sigma, \phi)} - 1 \right) \right], \quad (3)$$

where  $\beta \approx 3.37$  is the rate of decay<sup>57</sup> (Grunëissen parameter). The parameter  $\gamma_0 = 2.7 \text{ eV}$  is the interatomic hopping parameter for pristine graphene that we will set as  $\gamma_0 = 1$  in what follows, this is, all energies will be measured in units of  $\gamma_0$ . Thus  $\gamma_j$  will always be measured in units of  $\gamma_0$ . Finally the function  $f(j, \sigma, \phi)$  is defined as,

$$f(j, \sigma, \phi) = 2 \sin \left( \sqrt{3}\pi\sigma/2 \right) \sin \left[ \sqrt{3}\pi\sigma(j + 1/2) + \phi \right]. \quad (4)$$

The main features of this Hamiltonian have been described in a previous work, in the small strain's amplitude limit<sup>42</sup>. Let us make some remarks about the difference between considering zigzag or armchair graphene nanoribbons. As has been proven before, it is much easy to open a gap applying a strain field along the zigzag direction on an armchair graphene nanoribbon. Therefore, one expect that gaps emerge for certain parameters' values. In addition, one expect that edge states be very different from the ones that appear in the zigzag case, indeed this is the case as will be seen later on.

Once that the Hamiltonian of an uniaxial strained AGN have been presented, we now introduce the time dependence to the model. In particular, we consider the case of a short-time strain impulse that can be approximated as a delta kicking. A graphic description of the driving layout is shown in Fig. 1. Therein, we see that the deformation field is turned on at times  $t = mT$  where  $T$  is the driving period and  $m$  is an integer number. The strain is turned off whenever that  $t \neq mT$ . That is, we consider a time-dependent Hamiltonian of the following form

$$H(k_x, t) = H_0(k_x) + \sum_m [H_1(k_x) - H_0(k_x)] \delta(t/T - m), \quad (5)$$

with the Hamiltonians  $H_0$  and  $H_1$  given by,

$$H_0(k_x) = \sum_{j=1}^{N/2-1} \gamma_0 \left[ d(k_x) a_{2j}^\dagger b_{2j} + a_{2j-1}^\dagger b_{2j-1} \right] + \sum_{j=1}^{N/2-1} \gamma_0 a_j^\dagger b_{j+1} + \text{h.c.}, \quad (6)$$

and

$$H_1(k_x) = \sum_{j=1}^{N/2-1} \gamma_0 \left[ d(k_x) a_{2j}^\dagger b_{2j} + a_{2j-1}^\dagger b_{2j-1} \right] + \sum_{j=1}^{N/2-1} \gamma_j a_j^\dagger b_{j+1} + \text{h.c.} \quad (7)$$

Even though the experimental realization of the proposed driving layout is experimentally challenging, there are some proposed experiments for similar situations<sup>21,58</sup>.

To study the quasienergy spectrum we construct the one-period time evolution operator of the system, defined as<sup>59</sup>,

$$U(k_x, T) |\psi_{k_x}(t)\rangle = |\psi_{k_x}(t+T)\rangle, \quad (8)$$

where  $|\psi_{k_x}(t)\rangle$  is the time-dependent wave function of the system for a given momentum  $k_x$  along the  $x$ -axis. For the considered delta-kicking driving layout,  $U(k_x, T)$  can be written in a very simple manner, namely,

$$U(k_x, \tau) = \mathcal{T} \exp \left[ -i \int_0^\tau H(k_x, t) dt / \hbar \right] = \exp [-i\tau(H_1(k_x) - H_0(k_x))] \exp [-i\tau H_0(k_x)], \quad (9)$$

where  $\mathcal{T}$  denotes the time ordering operator and  $\tau = T/\hbar$ .

Even though the Hamiltonians  $H_1(k_x)$  and  $H_0(k_x)$  do not commute, we can study the eigenvalue spectrum of  $U(k_x, \tau)$  via an effective Hamiltonian defined as,

$$U(k_x, \tau) = \exp (-i\tau H_{\text{eff}}(k_x, \tau)) \quad (10)$$

The previous time evolution operator has eigenvalues  $\exp(-i\tau\omega)$ , where  $\tau\omega$  are called the quasienergies of the system. They are defined up to integer multiples of  $2\pi$ . After introducing the time-dependence to the model, there are four free parameters: three owing to the strain field ( $\lambda$ ,  $\sigma$ , and  $\phi$ ) and one to the driving ( $\tau$ ).

One can study the system for a wide range of parameters. Maybe the most important one is the value of  $\sigma$  since it controls the wavelength of the strain field. If this wavelength is incommensurate with respect to the graphene cell, the system is quasiperiodic resulting in a complex spectrum for the static undriven case. However, since topological states are observed only when translational invariance holds<sup>60</sup>, here we study only commensurate cases. In particular, we chose two different values

for  $\sigma$ , namely, 1)  $\sigma = 1/\sqrt{3}$  and 2)  $\sigma = 0.5/\sqrt{3}$ , setting  $\phi = \pi\sigma$  for each case. We have chosen such  $\sigma$  values since  $\sigma = 1/\sqrt{3}$  gives the smallest spatial period along the  $y$ -axis and the system is on a gapless phase around zero and  $\pm\pi$  quasienergy in the bulk spectrum. While for  $\sigma = 0.5/\sqrt{3}$  we obtain the next size of the spatial period and the system is gapped around zero quasienergy in the bulk spectrum.

For  $\sigma = 1/\sqrt{3}$  the supercell contains two rows of graphene in the  $y$  direction, or in other words, four inequivalent carbon atoms in the supercell, since the hopping parameters just take two different values, which are given by substituting the following expression

$$f(j, 1/\sqrt{3}, \phi) = 2\lambda(-1)^j \cos(\phi), \quad (11)$$

in Eq. (3). On the other hand, for  $\sigma = 1/2\sqrt{3}$  the hopping parameters takes four different values, meaning that now the supercell has eight inequivalent atoms. Once again, the hopping parameters are given by substituting the following expression,

$$f\left(j, \frac{1}{2\sqrt{3}}, \phi\right) = 2\lambda \sin\left[\frac{\pi}{2}(j+1/2)\right] \sin\left[\frac{\pi}{4} + (-1)^j \phi\right], \quad (12)$$

in Eq. (3). Note that for  $\sigma = 1/2\sqrt{3}$ , the periodicity of the system is doubled with respect to  $\sigma = 1/\sqrt{3}$  along the  $y$ -direction.

### III. QUASIENERGY SPECTRUM

In this section we will study the quasienergy spectrum and the emergence of topological edge states. We start by building the matrix representation of  $U(\tau)$  as described in Eq. (9). Then, their eigenvalues as a function of  $k_x$  are obtained by numerical calculations for a finite system. We consider a system with  $N = 324$  atoms per unit cell, this is the unit cell size used in all the cases presented here on. It is worthwhile that for  $\sigma = 1/\sqrt{3}$  or  $\sigma = 1/2\sqrt{3}$  the system becomes periodic in the  $y$ -direction. Therefore, by applying cyclic boundary conditions along the  $x$ - and  $y$ -directions, the quasienergy spectrum can be also obtained by Fourier transforming the Hamiltonians  $H_0(k_x)$  and  $H_1(k_x)$  and then substituting them into Eq. (9), however, no edge states appear in the quasienergy dispersion relation obtained by using this method. To observe such edge states, here we perform calculations in real space for the  $y$ -direction.

Let us start by studying the quasienergy spectrum for  $\sigma = 1/\sqrt{3}$ , in other words, the gapless quasienergy spectrum. In Fig. 2 we show the quasienergy band structure for  $\lambda = 0.2$ ,  $\tau = \pi$ ,  $\phi = \pi\sigma$ , and  $\sigma = 1/\sqrt{3}$ . In panel a) we have used cyclic boundary conditions, whereas for panel b) the boundary conditions were changed to fixed. Observe that the main difference between panel a) and b) is that in b) edge states emerge. The colors in the figure represent the logarithm of the normalized inverse

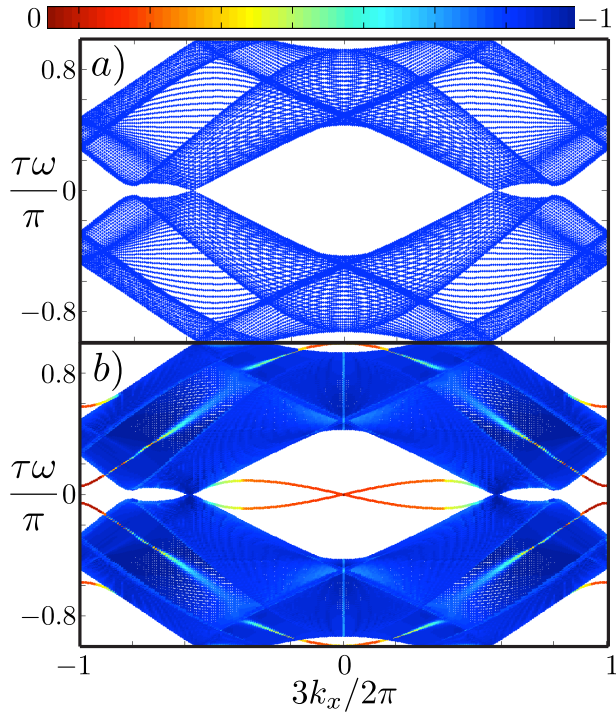


FIG. 2. (Color online). Gapless quasienergy band structure obtained from the numerical diagonalization of the matrix representation given by Eq. (9). The parameters used are  $\sigma = 1/\sqrt{3}$ ,  $\lambda = 0.2$ ,  $\tau = \pi$ ,  $\phi = \pi\sigma$ , and  $N = 324$ , for a) cyclic boundary conditions and b) fixed boundary conditions. In Panel a), note that no edge states appear since cyclic boundary conditions were used. In Panel b), two kinds of edge states emerge. Ones appear around zero quasienergy. The others are cosine-like edge states that merge and coexist with the bulk bands. The colors represent the inverse participation ratio. For red color the states are highly localized, whereas for blue color they are totally delocalized.

participation ratio (IPR) as defined in<sup>41</sup>. The IPR is a measured of the wave functions localization. The closer to zero the IPR (red color in figures) the more localized the wave function is. Delocalized or extended wave functions are labeled by blue color in figures, and correspond to IPR tending to  $-1$ .

It is interesting to note that even though the system is on a gapless phase, edge states appear. Moreover, two kinds of edge states are observed in Fig. 2. Ones around zero quasienergy, which are degenerate at  $k_x = 0$ , but decouple and delocalize as they move away from that point, following a cosine-like dispersion. The other ones also have a cosine-like dispersion and are degenerated at  $k_x = 0$  at  $\pm\pi$  quasienergy, however as they move away from that point they decouple and, eventually, they merge with the bulk bands without being totally delocalized states. We have numerically checked that they are localized near opposite edges of the AGN. Also, we stress out that the quasienergy spectrum strongly depends upon the phase  $\phi$  of the strain field. To see this point, in Fig. 3 we present the quasienergy band struc-

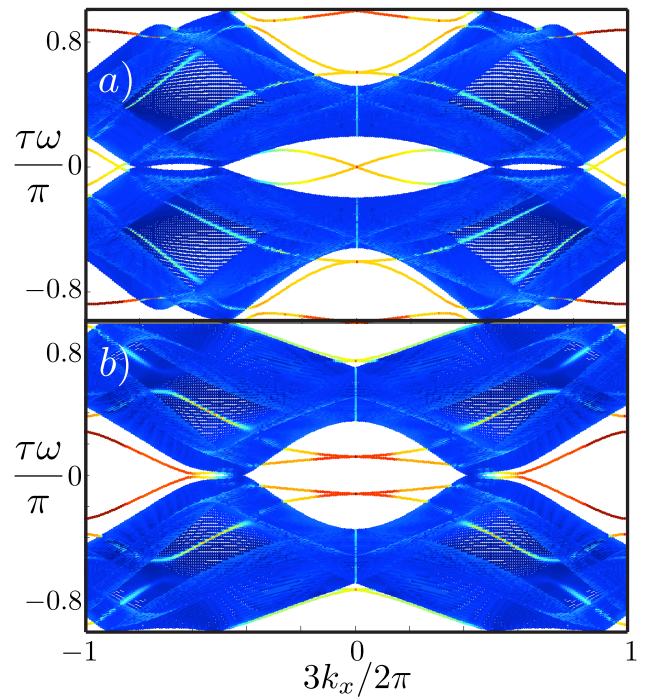


FIG. 3. (Color online). Gapless quasienergy band structure obtained from the numerical diagonalization of the matrix representation of Eq. (9). The parameters used are  $\sigma = 1/\sqrt{3}$ ,  $\lambda = 0.2$ ,  $\tau = \pi$ ,  $N = 324$ , and using fixed boundary conditions for a)  $\phi = 0$  and b)  $\phi = \pi\sigma/2$ . Note that for a) and b) panels the edge states deeply penetrate into the bulk bands. Also, for panel b), edge states around zero quasienergy are decoupled. It was used the same color code as in Fig. 2.

ture for:  $\phi = 0$  (panel a) and  $\phi = \pi\sigma/2$  (panel b). In panel a) of such figure, it can be seen that the edge states are quite similar to the ones shown in Fig. 2 b). However, the edge states in Fig. 3 a) deeply penetres into the bulk bands. Whereas, the edge states in Fig. 3 b) do not touch neither at zero nor at  $\pm\pi$  quasienergies when  $k_x = 0$ , instead a finite gap between them has been opened. Besides, they decouple into four bands around zero quasienergy, and also deeply penetres into the bulk states. The strong dependence of the quasienergy band structure on  $\phi$  can be explained as follows. Basically, the phase  $\phi$  determines how the strain pattern matches with the edges of the AGN, a fact that has been proven to be crucial in the topological properties of similar systems<sup>18,61</sup>. In the next section, we topologically characterize the edge states that emerge for  $\phi = \pi\sigma$ , we found that they are at least weak topologically non-trivial.

Due to topological edge states are very robust to small perturbations, we expect edge states not to be destroyed by a full gap in the bulk spectrum. To confirm this assertion, in Fig. 4 we plot the quasienergy band structure in a gapped phase of the system, this is, we used the same conditions as in Fig. 4 but using  $\sigma = 1/2\sqrt{3}$  for fixed boundary conditions. As can be seen the quasienergy



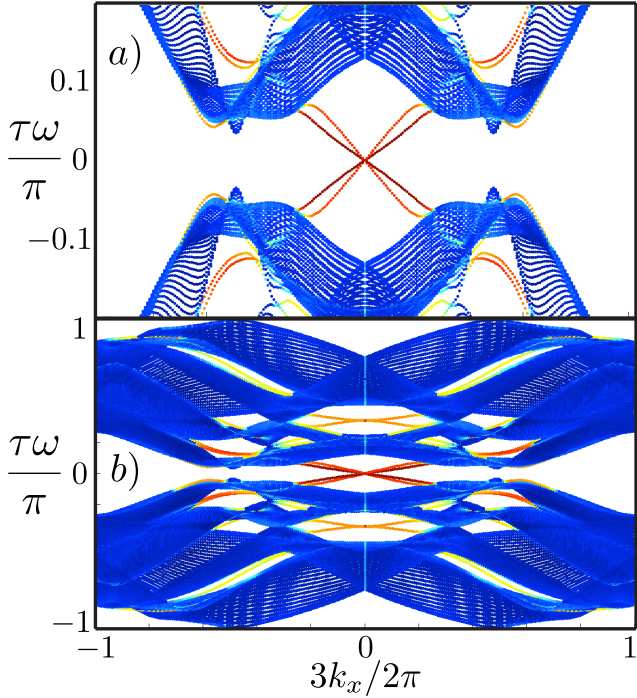


FIG. 4. (Color online). Gapful quasienergy band structure obtained from the numerical diagonalization of the matrix representation of Eq. (9) for  $\sigma = 1/2\sqrt{3}$ ,  $\lambda = 0.2$ ,  $\tau = \pi$ ,  $\phi = \pi\sigma$ , and  $N = 324$  using fixed boundary conditions. In panel a) we show an amplification around zero quasienergy to highlight the zero quasienergy edge modes that are shown. Observe that edge states also emerge at other gaps. The same color code as in Fig. 2 was used.

spectrum is on a gapped phase. Note that four edge states emerge around zero quasienergy, also note how they merge in a single point at  $k_x = 0$  as in Fig. 2. Besides that, other edge states emerge always that a partly gap appear on the quasienergy spectrum. Due to our model possesses chiral symmetry (this will be proven in the next section) the edges states that appear in the gap around zero quasienergy are topologically trivial<sup>55</sup>. However, edge states at other gaps (this is, full gaps not centered around zero or  $\pm\pi$  quasienergy) can be topologically non-trivial from the point of view of the Chern number<sup>55</sup>. It is interesting that although the topological invariant is zero, edge states emerge, such states can be, therefore, topologically weak<sup>62,63</sup>. On the other hand, nothing can be said about the edge states that appear at partly gaps on the spectrum, see Fig. 4. A detailed study of the topological properties of these edge states is beyond the aim of this article.

#### IV. TOPOLOGICAL PROPERTIES OF EDGE STATES

Before entering to the study of the topological properties of the system, let us write the Fourier trans-

formed version of the Hamiltonians  $H_1(k_x)$  and  $H_0(k_x)$ , for  $\sigma = 1/\sqrt{3}$ . For periodic boundary conditions, the system becomes periodic in the  $y$ -direction, therefore it is possible to write the Hamiltonians  $H_1(k_x)$  and  $H_0(k_x)$  in reciprocal space by taken into account the periodicity in  $y$ -direction. This leads to a new quantum number  $k_y$ , from where it follows that  $H_1(k_x)$  and  $H_0(k_x)$  can be simplified using a suitable Fourier transform. In fact, it can be proven that such Hamiltonians are reduced to a  $4Q \times 4Q$  matrix dependent on  $\mathbf{k} = (k_x, k_y)$ , and  $Q$  is related to  $\sigma = P/(\sqrt{3}Q)$ . For the case  $\sigma = 1/\sqrt{3}$ , the matrices have its lowest size since  $Q = 1$ , therefore the matrices representing the Hamiltonians  $H_1(\mathbf{k})$  and  $H_0(\mathbf{k})$  are  $4 \times 4$ . This is the most simple case and the only one to be studied in what follows.

By writing the Hamiltonians in the chiral basis (the chiral basis is a basis that expresses the chiral symmetry of the system) one obtains,

$$\mathbb{H}_l(\mathbf{k}) = \begin{bmatrix} 0 & \tilde{\mathbb{H}}_l(\mathbf{k}) \\ \tilde{\mathbb{H}}_l^\dagger(\mathbf{k}) & 0 \end{bmatrix}, \quad (13)$$

where  $l = 0, 1$  and the tilde indicates  $2 \times 2$  matrices. The explicit form of  $\tilde{\mathbb{H}}_l(\mathbf{k})$  is given in appendix A. The perturbation  $\delta\mathbb{H}(k_y) = \mathbb{H}_1(\mathbf{k}) - \mathbb{H}_0(\mathbf{k})$  is simply written as,

$$\delta\mathbb{H}(k_y) = \begin{bmatrix} 0 & \delta\tilde{\mathbb{H}}(k_y) \\ \delta\tilde{\mathbb{H}}^\dagger(k_y) & 0 \end{bmatrix}, \quad (14)$$

where  $\delta\tilde{\mathbb{H}}(k_y) = \tilde{\mathbb{H}}_1(\mathbf{k}) - \tilde{\mathbb{H}}_0(\mathbf{k})$ . As before, the explicit form of these matrices is given in appendix A.

For studying the topological properties of our model we start by looking at the symmetries of the Hamiltonians  $\mathbb{H}_1(\mathbf{k})$  and  $\mathbb{H}_0(\mathbf{k})$ . Note that such Hamiltonians fulfill the following condition

$$\Gamma\mathbb{H}_l(\mathbf{k})\Gamma = -\mathbb{H}_l(\mathbf{k}) \quad (15)$$

where  $l = 0, 1$ . As a consequence, the Fourier transformed version of the time-dependent Hamiltonian Eq. (5) possesses the following property

$$\Gamma\mathbb{H}(\mathbf{k}, t)\Gamma = -\mathbb{H}(\mathbf{k}, -t) \quad (16)$$

where  $\Gamma$ , so called the chiral operator, is an unitary operator for which  $\Gamma^2 = \mathbb{I}_{4Q \times 4Q}$  ( $Q = 1$  for  $\sigma = 1/\sqrt{3}$ ), which can be represented, in the chiral basis, as

$$\Gamma = \begin{bmatrix} \mathbb{I}_{2Q \times 2Q} & 0 \\ 0 & -\mathbb{I}_{2Q \times 2Q} \end{bmatrix} \quad (17)$$

From Eq. (16) it follows that the Hamiltonian Eq. (5) is chiral, therefore, the time evolution operator Eq. (9) must satisfy the following condition

$$\Gamma\mathbb{U}(\tau)\Gamma = \mathbb{U}^{-1}(\tau) = \mathbb{U}^\dagger(\tau) = \mathbb{U}(-\tau), \quad (18)$$

where the time evolution operator is now given by,

$$\mathbb{U}(\tau) = e^{-i\tau\delta\mathbb{H}(\mathbf{k})}e^{-i\tau\mathbb{H}_0(\mathbf{k})}. \quad (19)$$

Due to the condition Eq. (18) the quasienergy spectrum is symmetric respect to reflections along the  $k_x$ -axis, as is confirmed in Figs. 2, 3, and 4. Moreover, the chiral symmetry, for fully gapped systems in two dimensions, imposes the vanishing of the topological invariant at full gaps centered around zero and  $\pm\pi$  quasienergy. However, other gaps can be topologically non-trivial. As was mentioned before, for the case  $\sigma = 1/2\sqrt{3}$ , although the topological invariant is zero, edge states emerge in the gap centered at zero quasienergy, see Fig. 4. This implies that a different topological invariant is needed to topologically characterize the system or that the edge states are topologically weak<sup>62</sup>. On the other hand, for the gapless phase of the system, we cannot say nothing about the topology nature of the edge states just by looking at the symmetries of the time evolution  $\mathbb{U}(\tau)$ . Therefore, to topologically characterize the edge states that emerge in the gapless phase of our system (see Fig. 2), we study the topological properties of a one-dimensional slide of the two-dimensional system, *i.e.*, we consider the case  $k_x = 0$ . As we will see in what follows, this one dimensional slide is topologically non-trivial.

## V. ANALYTICAL STUDY OF THE CASE

$$\sigma = 1/\sqrt{3} \text{ AT } k_x = 0$$

We begin studying the emergence of edge states. For doing that, note that edge states will emerge for the first time when the lower and upper quasienergy band edges cross each other as  $\tau$  is increased from zero, keeping the other parameters fixed. For obtaining the quasienergy band edges note that the extreme values of the quasienergy spectrum, for a time evolution operator like the one in Eq. (19), are reached when the Hamiltonians  $\mathbb{H}_0$  and  $\delta\mathbb{H}$  commute, let us denote  $k_x^*$  and  $k_y^*$  the points at where this happens. From Eq. (A5), we can readily obtain that  $k_x^* = 3n\pi/2$  and  $k_y^* = n\pi/\sqrt{3}$ , where  $n$  is an integer number. Since we are interested in study a one-dimensional slide of our system, we chose first consider  $k_x = 0$  and study the quasienergy spectrum as a function of  $k_y$ . As is proven in appendix B, for  $k_x = 0$ , the time evolution operator becomes block diagonal,

$$\mathbb{U}'(\tau) = \begin{bmatrix} e^{i\tau\delta\tilde{h}(k_y)}e^{i\tau\tilde{h}_0(k_y)} & 0 \\ 0 & e^{-i\tau\delta\tilde{h}(k_y)}e^{-i\tau\tilde{h}_0(k_y)} \end{bmatrix} \quad (20)$$

where  $\mathbb{U}'(\tau)$  is the time evolution operator Eq. (19) in the basis at where  $\mathbb{H}_0$  is diagonal, see the appendix for details.  $\delta\tilde{h}(k_y)$  and  $\tilde{h}_0(k_y)$  can be written as follows,

$$\begin{aligned} \delta\tilde{h}(k_y) &= \delta h(k_y) \delta\hat{\mathbf{h}} \cdot \sigma, \\ \tilde{h}_0(k_y) &= \mathbb{I}_{2 \times 2} + 2 \cos\left(\sqrt{3}k_y/2\right)\sigma_z, \end{aligned} \quad (21)$$

where  $\sigma = (\sigma_x, \sigma_y, \sigma_z)$ ,  $\sigma_i$  ( $i = x, y, z$ ) is the  $2 \times 2$  Pauli matrix, and the components of  $\delta\hat{\mathbf{h}}$  are given by,

$$\begin{aligned} \delta h^{(y)} &= (\gamma_1 - \gamma_2) \sin\left(\sqrt{3}k_y/2\right), \\ \delta h^{(z)} &= (\gamma_1 + \gamma_2 - 2) \cos\left(\sqrt{3}k_y/2\right), \end{aligned} \quad (22)$$

also we define the norm  $\delta h(k_y)$  as

$$\delta h(k_y) = \sqrt{[\delta h^{(y)}]^2 + [\delta h^{(z)}]^2}. \quad (23)$$

Now, it is possible to analytically obtain the quasienergies of  $\mathbb{U}'(\tau)$  by studying one block at time. We will do that via an effective Hamiltonian defined as,

$$e^{i\tau\tilde{h}_{\text{eff}}(k_y)} = e^{i\tau\delta\tilde{h}(k_y)}e^{i\tau\tilde{h}_0(k_y)} \quad (24)$$

For calculating  $\tilde{h}_{\text{eff}}$  we use the addition rule of  $\text{SU}(2)$ , after some algebraic operations, detailed in the appendix, one gets,

$$\tilde{h}_{\text{eff}}(k_y) = \mathbb{I}_{2 \times 2} + \omega(k_y)\hat{\mathbf{h}}_{\text{eff}} \cdot \sigma \quad (25)$$

where  $\hat{\mathbf{h}}_{\text{eff}}$  is a unit vector defined in appendix B. Finally,  $\tau\omega(k_y)$  can be written as,

$$\begin{aligned} \cos[\tau\omega(k_y)] &= \cos(\tau\delta h) \cos\left[2\tau \cos\left(\sqrt{3}k_y/2\right)\right] \\ &\quad - \hat{e}_z \cdot \delta\hat{\mathbf{h}} \sin(\tau\delta h) \sin\left[2\tau \cos\left(\sqrt{3}k_y/2\right)\right]. \end{aligned} \quad (26)$$

It is important to remark that the quasienergies are not given by  $\pm\tau\omega(k_y)$  but by  $\pm\tau\omega_{\text{eff}}(k_y)$ , with

$$\tau\omega_{\text{eff}}(k_y) = \tau[\pm 1 + \omega(k_y)]. \quad (27)$$

The topological information of the system, for  $\sigma = 1/\sqrt{3}$  and  $k_x = 0$ , is now contained in the effective Hamiltonian (25). However, it is illustrating to obtain the needed conditions for having edge states before studying the topological properties of Hamiltonian (25). Since edge states will emerge when the lower and upper band edges cross each other at the first time, we begin by obtained such band edges. As we mentioned before, the extreme values of the quasienergy spectrum are found at  $k_x = k_x^* = 0$  and  $k_y = k_y^* = 0$ , after substituting such values in Eq. (26) one gets,

$$\tau\omega_{\pm} = \tau(\pm 1 + \gamma_1 + \gamma_2). \quad (28)$$

Now, the condition for having quasienergy band edge crossings is given by,

$$\tau_c(\omega_+ \pm \omega_-) = 2\pi. \quad (29)$$

By using Eq. (28) we obtain,

$$\begin{aligned} \tau_c^+ &= \frac{\pi}{\gamma_1 + \gamma_2}, \\ \tau_c^- &= \pi. \end{aligned} \quad (30)$$

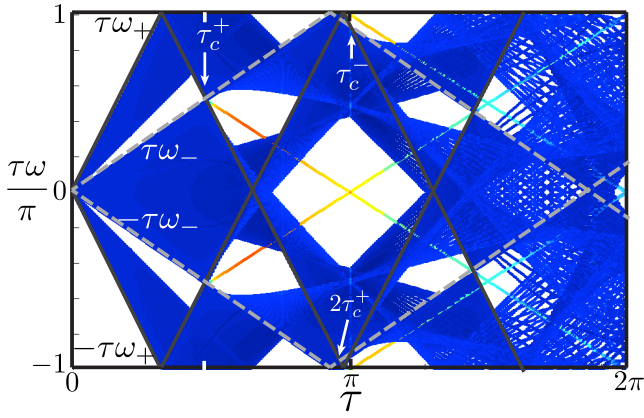


FIG. 5. (Color online). Quasienergy band spectrum for  $k_x = 0$  as a function of  $\tau$  obtained by numerical diagonalization of Eq. (9) using  $N = 324$ ,  $\sigma = 1/\sqrt{3}$ ,  $\lambda = 0.2$ ,  $\phi = \pi\sigma$ , and fixed boundary conditions. The quasienergy band edge  $\tau\omega^+$  ( $\tau\omega^-$ ) is denoted by solid black (dotted gray) lines. Note that such band edges cross each other for the first time at  $\tau = \tau_c^+$  at quasienergies different from zero or  $\pm\pi$ . It is interesting that at  $\tau_c^+$  edge states emerge, however for  $\tau_c^-$  not. Also, observe that the edge states are no flat bands but they depend linearly on  $\tau$ . See section V.

All other band crossings are given by  $m\tau_c^\pm$ , where  $m$  is an integer number. To shed light on the physics of the previous analysis, it is meaningful to see it graphically. In Fig. 5 we plot the quasienergy spectrum for  $k_x = 0$  as a function of  $\tau$  obtained by numerical diagonalization of Eq. (9) using  $N = 324$ ,  $\sigma = 1/\sqrt{3}$ ,  $\lambda = 0.2$ ,  $\phi = \pi\sigma$ , and fixed boundary conditions. Therein, the band edges  $\pm\tau\omega^+$  ( $\pm\tau\omega^-$ ) are denoted by solid black (dotted gray) lines, the critical values of  $\tau$  are displayed, as well. As can be seen, the edges  $\tau\omega^\pm$  start at zero for  $\tau = 0$ , as  $\tau$  is increased they start to grow linearly but with different slopes. Since  $\omega^+ \geq \omega^-$ ,  $\omega^+$  reaches first the limit of the first Floquet zone, if  $\tau$  is further increase  $\omega^+$  and  $\omega^-$  cross each other at  $\tau_c^+$ , by further increasing  $\tau$  a new band edge crossing emerge at  $\tau_c^-$ . Interestingly, the only crossings that produce edge states are the ones at  $\tau = m\tau_c^+$ . For the other crossings (at  $m\tau_c^-$ ) no gap is opened, hence no edge states emerge. Observe that for  $\tau_c^+$  the band edge crossings do not occur at zero or  $\pm\pi$  quasienergy, instead, they cross each other at,

$$\tau_c^+ \omega_\pm = \pi \pm \frac{\pi}{\gamma_1 + \gamma_2}. \quad (31)$$

Unlike the case of driven uniaxial strained zigzag graphene nanoribbons<sup>25</sup>, the quasienergy at which these edge states emerge is different from zero or  $\pm\pi$ . Moreover, the edge states for the case here considered (and for  $k_x = 0$ ) are not flat bands but unidirectional edge states, meaning that the quasienergy of such states grows linearly with  $\tau$ , see Fig. 5, where the edge states can be clearly seen. Note that as  $\tau$  is increased, the edge states start to delocalize. When  $\tau$  reaches  $2\pi$  they are almost completely extended, see Fig. 5, at where the colors rep-

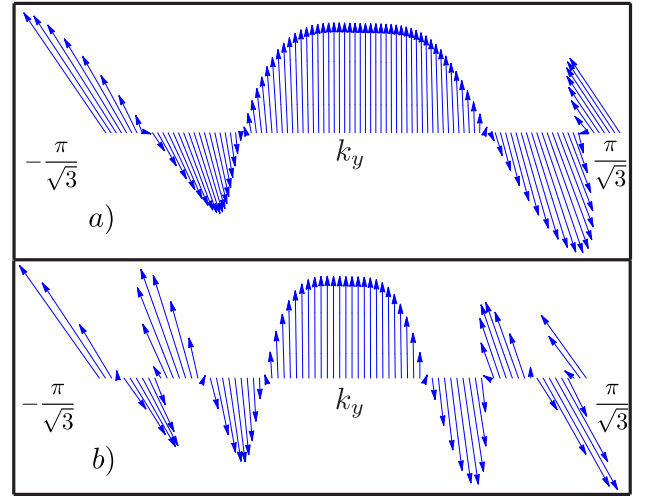


FIG. 6. (Color online). The winding of the vector  $\hat{\mathbf{h}}_{\text{eff}}(k_y)$  for  $k_x = 0$ ,  $\lambda = 0.2$ ,  $\sigma = 1/\sqrt{3}$ , and  $\phi = \pi\sigma$  using  $\tau = \pi$  for panel a) and  $\tau = 2\pi$  for panel b). Then, the winding number for panel a) is 2, whereas for panel b) is 4. Observe that by increasing the driving period  $\tau$ , the winding number is also increased.

resent the normalized inverse participation ratio.

To finish this section, we will show that these edge states for  $\tau$  and  $\lambda$  fixed are topologically non-trivial. That will be done by studying the effective Hamiltonian Eq. (25). For having topologically non-trivial properties the winding number of the unitary vector  $\hat{\mathbf{h}}_{\text{eff}}(k_y)$  around the origin must be non-vanishing. This is confirmed graphically in Fig. 6, therein, we show the winding of  $\hat{\mathbf{h}}_{\text{eff}}(k_y)$  for  $k_x = 0$ ,  $\lambda = 0.2$ ,  $\phi = \pi\sigma$ , and  $\sigma = 1/\sqrt{3}$ . As can be seen, the winding number for this particular case is 2. Hence, the system is topologically non-trivial for a one-dimensional slide at  $k_x = 0$ . This means that the edge states observed in Fig. 2 b) can have a topologically weak nature. However, a more detailed analysis is required to fully characterize the topological properties of our model, in both the gapless and the gapful phases.

## VI. CONCLUSIONS

We have observed the emergence of topological edge states in periodically driven uniaxial strained AGN. The system has a gapped phase (for  $\sigma = 1/\sqrt{3}$ ) and a gapless phase (for  $\sigma = 1/2\sqrt{3}$ ). For the gapped phase, highly localized edge states were found around zero quasienergy, which, due to the chirality of the system, must be topologically trivial from the Chern number point of view<sup>55</sup>. However, this phase also exhibits edge states at gaps at quasienergies different from zero or  $\pm\pi$  that could be topologically non-trivial, although a more detailed analysis is required. On the other hand, for the gapped phase of the system, we found the necessary conditions for the emergence of the edge states. Additionally, by studying

a one-dimensional slide of the case system at  $k_x = 0$ , we were able to analytically obtain the quasienergy spectrum of such slide, since for this case the time evolution operator can be effectively describe by a block diagonal  $4 \times 4$  matrix, in other words, we obtained the effective Hamiltonian for  $k_x = 0$ . After looking at the topological properties of the effective Hamiltonian, we found that the edge states for this slide are topologically non-trivial. Although, a deeper analysis is needed, we can say that the edge states observed in the case  $\sigma = 1/\sqrt{3}$  have, at least, a topologically weak nature. We hope that our work motives further research about the case here presented.

This project was supported by DGAPA-PAPIIT Project 102717. P. R.-T. acknowledges financial support from Consejo Nacional de Ciencia y Tecnología (CONACYT) (México). We gratefully thank M. Fruchart for helpful discussions.

### Appendix A

Let us now compute the unitary operator  $\mathbb{U}(\tau)$ . Before entering into the detailed calculation, we first define the Hamiltonians  $\mathbb{H}_0$  and  $\mathbb{H}_1$ ,

$$\mathbb{H}_l(\mathbf{k}) = \begin{bmatrix} 0 & \tilde{\mathbb{H}}_l(\mathbf{k}) \\ \tilde{\mathbb{H}}_l^\dagger(\mathbf{k}) & 0 \end{bmatrix}, \quad (\text{A1})$$

the label  $l$  can take the values  $l = 0, 1$ , and

$$\begin{aligned} \tilde{\mathbb{H}}_0(\mathbf{k}) &= \begin{bmatrix} 1 & 1 + e^{-i\sqrt{3}k_y} \\ 1 + e^{i\sqrt{3}k_y} & e^{-i3k_x} \end{bmatrix}, \\ \tilde{\mathbb{H}}_1(\mathbf{k}) &= \begin{bmatrix} 1 & \gamma_1 + \gamma_2 e^{-i\sqrt{3}k_y} \\ \gamma_1 + \gamma_2 e^{i\sqrt{3}k_y} & e^{-i3k_x} \end{bmatrix}. \end{aligned} \quad (\text{A2})$$

Then, the perturbed Hamiltonian defined as  $\delta\mathbb{H} = \mathbb{H}_1(\mathbf{k}) - \mathbb{H}_0(\mathbf{k})$  takes the form,

$$\delta\mathbb{H}(k_y) = \begin{bmatrix} 0 & \delta\tilde{\mathbb{H}}(k_y) \\ \delta\tilde{\mathbb{H}}(k_y) & 0 \end{bmatrix}, \quad (\text{A3})$$

with

$$\delta\tilde{\mathbb{H}}(k_y) = \begin{bmatrix} 0 & \delta_1 + \delta_2 e^{-i\sqrt{3}k_y} \\ \delta_1 + \delta_2 e^{i\sqrt{3}k_y} & 0 \end{bmatrix}, \quad (\text{A4})$$

where  $\delta_{1,2} = \gamma_{1,2} - 1$ . Note that the unperturbed and perturbed Hamiltonians do not commute. In fact, we have

$$[\delta\mathbb{H}(k_y), \mathbb{H}(\mathbf{k})] = \begin{bmatrix} \tilde{\mathbb{C}}(\mathbf{k}) & 0 \\ 0 & \tilde{\mathbb{C}}(\mathbf{k}) \end{bmatrix}, \quad (\text{A5})$$

where

$$\begin{aligned} \tilde{\mathbb{C}}(\mathbf{k}) &= 2i(\gamma_1 - \gamma_2) \sin(\sqrt{3}k_y) \sigma_z \\ &+ 2 \left[ \delta_1 \sin\left(\frac{3k_x}{2}\right) + \delta_2 \sin\left(\frac{3k_x}{2} - \sqrt{3}k_y\right) \right] \\ &\times \sin\left(\frac{3k_x}{2}\right) \sigma_x + \\ &2 \left[ \delta_1 \cos\left(\frac{3k_x}{2}\right) + \delta_2 \cos\left(\frac{3k_x}{2} - \sqrt{3}k_y\right) \right] \\ &\times \sin\left(\frac{3k_x}{2}\right) \sigma_y \end{aligned} \quad (\text{A6})$$

where  $\sigma_{x,y}$  are the  $2 \times 2$  Pauli matrices and  $\delta_{1,2} = \gamma_{1,2} - 1$  as before.

For obtaining the time evolution operator, we start by finding the eigenvalues and eigenvectors of the pristine system described by  $\mathbb{H}_0(\mathbf{k})$ . These eigenvalues are readily found by renormalizing one of the bipartite sublattices, since it is equivalent to consider the squared matrix  $\mathbb{H}_0(\mathbf{k})^2$ , as shown in references<sup>64,65</sup>. Thus, the eigenvalues of  $\mathbb{H}_0(\mathbf{k})$ , denoted by  $E_{1,2}(k_x, k_y)$  are,

$$\begin{aligned} E_1(k_x, k_y) &= \\ &\pm \sqrt{3 + 4 \cos(3k_x/2) \cos(\sqrt{3}k_y/2) + 2 \cos(\sqrt{3}k_y)}, \\ E_2(k_x, k_y) &= \\ &\pm \sqrt{3 - 4 \cos(3k_x/2) \cos(\sqrt{3}k_y/2) + 2 \cos(\sqrt{3}k_y)}. \end{aligned} \quad (\text{A7})$$

To find the unitary transformation that diagonalizes  $\mathbb{H}_0(\mathbf{k})$ , care must be taken since the eigenvalues of  $\mathbb{H}_0(\mathbf{k})^2$  are degenerate and thus are not necessarily eigenvectors of  $\mathbb{H}_0(\mathbf{k})$ . However, we observe that since the wavefunctions of  $\mathbb{H}_0(\mathbf{k})$  correspond to pristine graphene, one can apply the Bloch theorem for the original Brillouin zone of graphene to get the proper eigenfunctions. Using the well known solution for graphene and ordering the energies as  $E_1, E_2, -E_1, -E_2$ , we obtain the unitary transformation that diagonalizes  $\mathbb{H}_0(\mathbf{k})$ ,

$$O = \begin{bmatrix} \tilde{\mathbb{M}}_a & \tilde{\mathbb{M}}_a \\ \tilde{\mathbb{M}}_b & -\tilde{\mathbb{M}}_b \end{bmatrix} \quad (\text{A8})$$

where

$$\begin{aligned} \tilde{\mathbb{M}}_a(\mathbf{k}) &= \frac{1}{2} \begin{bmatrix} 1 & 1 \\ e^{-i\mathbf{k} \cdot \mathbf{a}_2} & -e^{-i\mathbf{k} \cdot \mathbf{a}_2} \end{bmatrix} \\ \tilde{\mathbb{M}}_b(\mathbf{k}) &= \frac{1}{2} \begin{bmatrix} e^{i\theta_1} & e^{i\theta_2} \\ e^{i\theta_1} e^{i\mathbf{k} \cdot \mathbf{a}_1} & -e^{i\theta_2} e^{i\mathbf{k} \cdot \mathbf{a}_1} \end{bmatrix}, \end{aligned} \quad (\text{A9})$$

$\mathbf{a}_1 = (3, \sqrt{3})/2$ ,  $\mathbf{a}_2 = (3, -\sqrt{3})/2$  being the lattice vectors of pristine graphene, and

$$\begin{aligned} e^{i\theta_1} &= \frac{1}{E_1} \left[ 1 + 2e^{-3ik_x/2} \cos(\sqrt{3}k_y/2) \right] \\ e^{i\theta_2} &= \frac{1}{E_2} \left[ 1 - 2e^{-3ik_x/2} \cos(\sqrt{3}k_y/2) \right]. \end{aligned} \quad (\text{A10})$$



The next step is to transform Eq. (9) onto the basis in which  $\mathbb{H}_0$  is diagonal, *i.e.*, to perform  $\mathbb{O}^\dagger \mathbb{U}(\tau) \mathbb{O} = \mathbb{U}'(\tau)$ . Before doing that, let us reduce  $\mathbb{U}(\tau)$  into a simpler form. To do that note that  $(\delta \mathbb{H})^2 = (\delta E(k_y))^2 \mathbb{I}_{4 \times 4}$ , where  $\mathbb{I}_{4 \times 4}$  is the  $4 \times 4$  identity matrix and

$$\delta E(k_y) = \sqrt{(\gamma_1 - 1)^2 + (\gamma_2 - 1)^2 + 2(\gamma_1 - 1)(\gamma_2 - 1) \cos(\sqrt{3}k_y)}. \quad (\text{A11})$$

As a result, the exponential of  $\delta \mathbb{H}$  can be written as

$$\exp[-i\tau(\delta H)] = \cos[\tau\delta E(k_y)]\mathbb{I} - i(\delta H) \frac{\sin[\tau\delta E(k_y)]}{\delta E(k_y)}, \quad (\text{A12})$$

and the time evolution operator becomes,

$$\mathbb{U}(\tau) = \left( \cos[\tau\delta E(k_y)] - i \frac{\sin[\tau\delta E(k_y)]}{\delta E(k_y)} \delta \mathbb{H}(k_y) \right) e^{-i\tau\mathbb{H}_0}. \quad (\text{A13})$$

Before transforming Eq. (9) into  $\mathbb{O}$ , we calculate  $\delta \mathbb{H}'(k_y) = \mathbb{O}^\dagger \delta \mathbb{H}(k_y) \mathbb{O}$ , after some algebraic operations, we get,

$$\delta \mathbb{H}' = \begin{bmatrix} \delta \tilde{\mathbb{H}}_+ & \delta \tilde{\mathbb{H}}_- \\ -\delta \tilde{\mathbb{H}}_- & -\delta \tilde{\mathbb{H}}_+ \end{bmatrix}, \quad (\text{A14})$$

where

$$\delta \tilde{\mathbb{H}}_\pm = \tilde{\mathbb{M}}_b^\dagger \delta \tilde{\mathbb{H}} \tilde{\mathbb{M}}_a \pm \tilde{\mathbb{M}}_a^\dagger \delta \tilde{\mathbb{H}} \tilde{\mathbb{M}}_b. \quad (\text{A15})$$

Finally, the time evolution operator is given by,

$$\mathbb{U}'(\tau) = -i \frac{\sin(\tau\delta E)}{\delta E} \times \begin{bmatrix} \left[ \cos(\tau\delta E) + \delta \tilde{\mathbb{H}}_+ \right] \tilde{\mathbb{U}}_0(\tau) & \delta \mathbb{H}_- \tilde{\mathbb{U}}_0^*(\tau) \\ -\delta \mathbb{H}_- \tilde{\mathbb{U}}_0(\tau) & \left[ \cos(\tau\delta E) - \delta \tilde{\mathbb{H}}_+ \right] \tilde{\mathbb{U}}_0^*(\tau) \end{bmatrix} \quad (\text{A16})$$

where  $\mathbb{U}'(\tau) = \mathbb{O}^\dagger(\mathbf{k}) \mathbb{U}(\tau) \mathbb{O}(\mathbf{k})$  and

$$\tilde{\mathbb{U}}_0(\tau) = \begin{bmatrix} e^{i\tau E_1} & 0 \\ 0 & e^{i\tau E_2} \end{bmatrix}. \quad (\text{A17})$$

## Appendix B: Particular case $k_x = 0$

For  $k_x = 0$  the time evolution operator operator  $\mathbb{U}'(\tau)$  becomes block diagonal, each block being a  $2 \times 2$  matrix.

Hence, the time evolution operator, Eq. (A16), can be written as,

$$\mathbb{U}'(\tau) = \begin{bmatrix} e^{i\tau\delta\tilde{h}(k_y)} e^{i\tau\tilde{h}_0(k_y)} & 0 \\ 0 & e^{-i\tau\delta\tilde{h}(k_y)} e^{-i\tau\tilde{h}_0(k_y)} \end{bmatrix} \quad (\text{B1})$$

where

$$\begin{aligned} \delta\tilde{h}(k_y) &= \delta E(k_y) \delta \hat{\mathbf{h}} \cdot \sigma, \\ \tilde{h}_0(k_y) &= \mathbb{I}_{2 \times 2} + 2 \cos(\sqrt{3}k_y/2) \sigma_z, \end{aligned} \quad (\text{B2})$$

with  $\sigma = (\sigma_x, \sigma_y, \sigma_z)$ ,  $\sigma_i$  ( $i = x, y, z$ ) being the  $2 \times 2$  Pauli matrices written in the basis at where  $\sigma_z$  is diagonal,  $\mathbb{I}_{2 \times 2}$  the  $2 \times 2$  identity matrix,  $\delta E(k_y)$  defined as in Eq. (A11), and the components of  $\delta \mathbf{h}$  are

$$\begin{aligned} \delta h^{(y)} &= (\gamma_1 - \gamma_2) \sin(\sqrt{3}k_y/2), \\ \delta h^{(z)} &= (\gamma_1 + \gamma_2 - 2) \cos(\sqrt{3}k_y/2). \end{aligned} \quad (\text{B3})$$

By using the addition rule of SU(2), Eq. (B1) can be written as follows,

$$\mathbb{U}'(\tau) = \begin{bmatrix} e^{i\tau\tilde{h}_{\text{eff}}(k_y)} & 0 \\ 0 & e^{-i\tau\tilde{h}_{\text{eff}}(k_y)} \end{bmatrix} \quad (\text{B4})$$

where

$$\tilde{h}_{\text{eff}}(k_y) = \mathbb{I}_{2 \times 2} + \omega(k_y) \hat{\mathbf{h}}_{\text{eff}} \cdot \sigma, \quad (\text{B5})$$

$\omega(k_y)$  is given by

$$\begin{aligned} \cos[\tau\omega(k_y)] &= \cos(\tau\delta E) \cos\left[2\tau \cos(\sqrt{3}k_y/2)\right] \\ &- \frac{\delta h^{(z)}}{\delta E} \sin(\tau\delta E) \sin\left[2\tau \cos(\sqrt{3}k_y/2)\right]. \end{aligned} \quad (\text{B6})$$

Finally, the unit vector  $\hat{\mathbf{h}}_{\text{eff}}$  is

$$\begin{aligned} \hat{\mathbf{h}}_{\text{eff}} &= \frac{1}{\sin[\tau\omega(k_y)]} \left( \delta \hat{\mathbf{h}} \sin(\tau\delta E) \cos\left[2\tau \cos(\sqrt{3}k_y/2)\right] \right. \\ &+ \hat{e}_z \cos(\tau\delta E) \sin\left[2\tau \cos(\sqrt{3}k_y/2)\right] \\ &\left. - \delta h^{(y)} \hat{e}_x \sin(\tau\delta E) \sin\left[2\tau \cos(\sqrt{3}k_y/2)\right] \right). \end{aligned} \quad (\text{B7})$$

It is noteworthy that the quasienergies of the system are not  $\pm\tau\omega(k_y)$  but  $\pm\tau(\pm 1 + \omega(k_y))$ , see the main text.

\* pedro.roman.taboada@gmail.com

<sup>1</sup> X.-L. Qi and S.-C. Zhang, Rev. Mod. Phys. **83**, 1057

(2011).

<sup>2</sup> C. Nayak, S. H. Simon, A. Stern, M. Freedman, and

- S. Das Sarma, *Rev. Mod. Phys.* **80**, 1083 (2008).
- <sup>3</sup> N. Ma, *Physica B: Condensed Matter* **512**, 100 (2017).
  - <sup>4</sup> I. Žutić, J. Fabian, and S. Das Sarma, *Rev. Mod. Phys.* **76**, 323 (2004).
  - <sup>5</sup> T. Yokoyama and S. Murakami, *Physica E: Low-dimensional Systems and Nanostructures* **55**, 1 (2014), topological Objects.
  - <sup>6</sup> C.-T. Wu, B. M. Anderson, W.-H. Hsiao, and K. Levin, *Phys. Rev. B* **95**, 014519 (2017).
  - <sup>7</sup> J. E. Moore, *Nature* **464**, 194 (2010).
  - <sup>8</sup> Y. L. Chen, J. G. Analytis, J.-H. Chu, Z. K. Liu, S.-K. Mo, X. L. Qi, H. J. Zhang, D. H. Lu, X. Dai, Z. Fang, S. C. Zhang, I. R. Fisher, Z. Hussain, and Z.-X. Shen, *Science* **325**, 178 (2009), <http://science.sciencemag.org/content/325/5937/178.full.pdf>.
  - <sup>9</sup> I. I. Satija and G. G. Naumis, *Phys. Rev. B* **88**, 054204 (2013).
  - <sup>10</sup> J. C. Avila, H. Schulz-Baldes, and C. Villegas-Blas, *Mathematical Physics, Analysis and Geometry* **16**, 137 (2013).
  - <sup>11</sup> J. Cayssol, B. Dra, F. Simon, and R. Moessner, *physica status solidi (RRL) Rapid Research Letters* **7**, 101 (2013).
  - <sup>12</sup> M. Thakurathi, A. A. Patel, D. Sen, and A. Dutta, *Phys. Rev. B* **88**, 155133 (2013).
  - <sup>13</sup> G. Usaj, P. M. Perez-Piskunow, L. E. F. Foa Torres, and C. A. Balseiro, *Phys. Rev. B* **90**, 115423 (2014).
  - <sup>14</sup> M. Thakurathi, K. Sengupta, and D. Sen, *Phys. Rev. B* **89**, 235434 (2014).
  - <sup>15</sup> H. Dehghani and A. Mitra, *Phys. Rev. B* **92**, 165111 (2015).
  - <sup>16</sup> C. Yuce, *The European Physical Journal D* **69**, 184 (2015).
  - <sup>17</sup> N. Sedlmayr, J. M. Aguiar-Hualde, and C. Bena, *Phys. Rev. B* **91**, 115415 (2015).
  - <sup>18</sup> V. Dal Lago, M. Atala, and L. E. F. Foa Torres, *Phys. Rev. A* **92**, 023624 (2015).
  - <sup>19</sup> N. Sedlmayr, J. M. Aguiar-Hualde, and C. Bena, *Phys. Rev. B* **93**, 155425 (2016).
  - <sup>20</sup> H. Dehghani and A. Mitra, *Phys. Rev. B* **93**, 245416 (2016).
  - <sup>21</sup> A. Agarwala, U. Bhattacharya, A. Dutta, and D. Sen, *Phys. Rev. B* **93**, 174301 (2016).
  - <sup>22</sup> Bhattacharya, Utso, Dasgupta, Sayak, and Dutta, Amit, *Eur. Phys. J. B* **89**, 216 (2016).
  - <sup>23</sup> R. S. Akzyanov, A. L. Rakhmanov, A. V. Rozhkov, and F. Nori, *Phys. Rev. B* **94**, 125428 (2016).
  - <sup>24</sup> A. Agarwala and V. B. Shenoy, *Phys. Rev. Lett.* **118**, 236402 (2017).
  - <sup>25</sup> P. Roman-Taboada and G. G. Naumis, *Phys. Rev. B* **95**, 115440 (2017).
  - <sup>26</sup> T. Kitagawa, E. Berg, M. Rudner, and E. Demler, *Phys. Rev. B* **82**, 235114 (2010).
  - <sup>27</sup> T. Kitagawa, M. A. Broome, A. Fedrizzi, M. S. Rudner, E. Berg, I. Kassal, A. Aspuru-Guzik, E. Demler, and A. G. White, **3**, 882 EP (2012).
  - <sup>28</sup> L. Jiang, T. Kitagawa, J. Alicea, A. R. Akhmerov, D. Pekker, G. Refael, J. I. Cirac, E. Demler, M. D. Lukin, and P. Zoller, *Phys. Rev. Lett.* **106**, 220402 (2011).
  - <sup>29</sup> B. M. Fregoso, Y. H. Wang, N. Gedik, and V. Galitski, *Phys. Rev. B* **88**, 155129 (2013).
  - <sup>30</sup> M. Benito, A. Gómez-León, V. M. Bastidas, T. Brandes, and G. Platero, *Phys. Rev. B* **90**, 205127 (2014).
  - <sup>31</sup> T. Iadecola, T. Neupert, and C. Chamon, *Phys. Rev. B* **89**, 115425 (2014).
  - <sup>32</sup> R. W. Bomantara, G. N. Raghava, L. Zhou, and J. Gong, *Phys. Rev. E* **93**, 022209 (2016).
  - <sup>33</sup> T. Ochiai, *Journal of Physics: Condensed Matter* **28**, 425501 (2016).
  - <sup>34</sup> T. T. Heikkilä, N. B. Kopnin, and G. E. Volovik, *JETP Letters* **94**, 233 (2011).
  - <sup>35</sup> A. P. Schnyder, S. Ryu, A. Furusaki, and A. W. W. Ludwig, *Phys. Rev. B* **78**, 195125 (2008).
  - <sup>36</sup> G. M. Graf and M. Porta, *Communications in Mathematical Physics* **324**, 851 (2013).
  - <sup>37</sup> D. Carpentier, P. Delplace, M. Fruchart, K. Gawdzki, and C. Tauber, *Nuclear Physics B* **896**, 779 (2015).
  - <sup>38</sup> F. Nathan and M. S. Rudner, *New Journal of Physics* **17**, 125014 (2015).
  - <sup>39</sup> G. E. Volovik, *Journal of Superconductivity and Novel Magnetism* **26**, 2887 (2013).
  - <sup>40</sup> M. Oliva-Leyva and G. G. Naumis, *Journal of Physics: Condensed Matter* **26**, 125302 (2014).
  - <sup>41</sup> G. G. Naumis and P. Roman-Taboada, *Phys. Rev. B* **89**, 241404 (2014).
  - <sup>42</sup> P. Roman-Taboada and G. G. Naumis, *Phys. Rev. B* **90**, 195435 (2014).
  - <sup>43</sup> M. Oliva-Leyva and G. G. Naumis, *2D Materials* **2**, 025001 (2015).
  - <sup>44</sup> P. Roman-Taboada and G. G. Naumis, *Phys. Rev. B* **92**, 035406 (2015).
  - <sup>45</sup> Y. Hatsugai, *Solid State Communications* **149**, 1061 (2009), recent Progress in Graphene Studies.
  - <sup>46</sup> P. Delplace, D. Ullmo, and G. Montambaux, *Phys. Rev. B* **84**, 195452 (2011).
  - <sup>47</sup> P. San-Jose, J. L. Lado, R. Aguado, F. Guinea, and J. Fernández-Rossier, *Phys. Rev. X* **5**, 041042 (2015).
  - <sup>48</sup> J. Feilhauer, W. Apel, and L. Schweitzer, *Phys. Rev. B* **92**, 245424 (2015).
  - <sup>49</sup> P. Delplace, A. Gómez-León, and G. Platero, *Phys. Rev. B* **88**, 245422 (2013).
  - <sup>50</sup> M. Oliva-Leyva and G. G. Naumis, *Journal of Physics: Condensed Matter* **28**, 025301 (2016).
  - <sup>51</sup> Z. Yan and Z. Wang, *Phys. Rev. Lett.* **117**, 087402 (2016).
  - <sup>52</sup> Dutreix, Clment, Guigou, Marine, Chevallier, Denis, and Bena, Cristina, *Eur. Phys. J. B* **87**, 296 (2014).
  - <sup>53</sup> V. M. Pereira, A. H. Castro Neto, and N. M. R. Peres, *Phys. Rev. B* **80**, 045401 (2009).
  - <sup>54</sup> M. O.-L. H. T. Gerardo G Naumis, Salvador Barraza-Lopez, arXiv:1611.08627.
  - <sup>55</sup> M. Fruchart, *Phys. Rev. B* **93**, 115429 (2016).
  - <sup>56</sup> A. Cresti, N. Nemec, B. Biel, G. Niebler, F. Triozon, G. Cuniberti, and S. Roche, *Nano Research* **1**, 361 (2008).
  - <sup>57</sup> M. Oliva-Leyva and G. G. Naumis, *Phys. Rev. B* **88**, 085430 (2013).
  - <sup>58</sup> T. Mishra, T. G. Sarkar, and J. N. Bandyopadhyay, *The European Physical Journal B* **88**, 231 (2015).
  - <sup>59</sup> M. S. Rudner, N. H. Lindner, E. Berg, and M. Levin, *Phys. Rev. X* **3**, 031005 (2013).
  - <sup>60</sup> S. Rao, arXiv:1603.02821.
  - <sup>61</sup> W. P. Su, J. R. Schrieffer, and A. J. Heeger, *Phys. Rev. Lett.* **42**, 1698 (1979).
  - <sup>62</sup> Y. Yoshimura, K.-I. Imura, T. Fukui, and Y. Hatsugai, *Phys. Rev. B* **90**, 155443 (2014).
  - <sup>63</sup> D. Y. H. Ho and J. Gong, *Phys. Rev. B* **90**, 195419 (2014).
  - <sup>64</sup> G. G. Naumis, *Phys. Rev. B* **76**, 153403 (2007).
  - <sup>65</sup> J. E. Barrios-Vargas and G. G. Naumis, *Journal of Physics: Condensed Matter* **23**, 375501 (2011).